



## 2D and Slab Turbulent Cascade Rates in the Inner Heliosphere

L. Adhikari<sup>1</sup> , G. P. Zank<sup>1</sup> , L.-L. Zhao<sup>1</sup> , and D. Telloni<sup>2</sup> <sup>1</sup> Center for Space Plasma and Aeronomic Research (CSPAR), and Department of Space Science, University of Alabama in Huntsville, Huntsville, AL 35899, USA; [la0004@uah.edu](mailto:la0004@uah.edu)<sup>2</sup> National Institute for Astrophysics–Astrophysical Observatory of Torino Via Osservatorio 20, I-10025 Pino Torinese, Italy  
Received 2022 April 11; revised 2022 August 30; accepted 2022 September 13; published 2022 October 19

### Abstract

We present a theoretical and observational study of 2D and slab turbulence cascade (or heating) rates of transverse total turbulence energies, transverse cross helicity, transverse outward and inward Elsässer energy, transverse fluctuating magnetic energy density, and transverse fluctuating kinetic energy from the perihelion of the first Parker Solar Probe (PSP) orbit at  $\sim 36.6 R_{\odot}$  to Solar Orbiter (SolO) at  $\sim 177 R_{\odot}$ . We use the Adhikari et al. (2021a) approach to calculate the observed transverse turbulence heating rate, and the nearly incompressible magnetohydrodynamic (NI MHD) turbulence transport theory to calculate the theoretical turbulence cascade rate. We find from the 1 day long PSP measurements at  $66.5 R_{\odot}$ , and the SolO measurements at  $176.3 R_{\odot}$  that various transverse turbulent cascade rates increase with increasing angle, from  $10^{\circ}$  to  $98^{\circ}$ , between the mean solar wind speed and mean magnetic field ( $\theta_{\text{UB}}$ ), indicating that the 2D heating rate is largest in the inner heliosphere. Similarly, we find from the theoretical and observed results that the 2D heating rate is larger than the slab heating rate as a function of heliocentric distance. We present a comparison between the theoretical and observed 2D and slab turbulence cascade rates as a function of heliocentric distance.

*Unified Astronomy Thesaurus concepts:* [The Sun \(1693\)](#); [Interplanetary turbulence \(830\)](#); [Heliosphere \(711\)](#)

### 1. Introduction

Historically, interplanetary fluctuations have been described as either a superposition of pure Alfvén waves (Belcher & Davis 1971) or evidence of a turbulent solar wind (Coleman 1968). A fundamental characteristic of well-developed turbulence is the transfer of turbulent (kinetic + magnetic) energy from large scales to small scales. This is known as a turbulence cascade, and is one of the main candidates thought to be responsible for the solar wind heating/coronal heating. In this framework, the energy is injected at the largest scales (i.e., the energy-containing range), cascades through the inertial range, and is finally dissipated as heat energy on the dissipation scales. Theoretically, this picture has been successful in describing the nonadiabatic radial profile of the solar wind temperature from the base of the solar corona to the outer heliosphere (Matthaeus et al. 1999; Smith et al. 2006; Usmanov et al. 2011; Adhikari et al. 2015; Zank et al. 2018b; Nakanotani et al. 2020; Adhikari et al. 2021a).

The first theoretical exact law for incompressible hydrodynamics turbulence was derived from the von Kármán–Howarth dynamical equation (von Karman & Howarth 1938). The exact laws are based on the zeroth law of turbulence which states that for fixed forcing, the rate of energy dissipation  $\epsilon \rightarrow 0$  as the viscosity  $\nu \rightarrow 0$ . The exact law gives an expression for the energy dissipation or cascade rate  $\epsilon$  as a function of the structure function of the turbulent fields (Monin & Yaglom 1971). Politano & Pouquet (1998a, 1998b) generalized the hydrodynamic exact laws to a magnetized plasma, such as the solar wind. The Politano–Pouquet third-order law (Politano & Pouquet 1998a, 1998b) calculates the transfer of turbulent energy through the inertial range, and has been used

by several authors to estimate cascade rates in the solar wind (Vasquez et al. 2007; MacBride et al. 2008; Smith et al. 2009; Podesta 2011; Bandyopadhyay et al. 2018, 2020; Pine et al. 2020; Smith & Vasquez 2021; Zhao et al. 2022b). Several generalized exact laws were also derived for compressible magnetohydrodynamic (MHD) turbulence (e.g., Galtier & Banerjee 2011; Andrés et al. 2019; Hellinger et al. 2021).

Most of the studies have focused on the study of the isotropic turbulent cascade rate. However, in the presence of a magnetic field, the turbulence power in a direction perpendicular to the mean magnetic field is different from that in the parallel direction (Matthaeus et al. 1990; Zank & Matthaeus 1992, 1993; Bieber et al. 1996; Saur & Bieber 1999; Forman et al. 2011; Zank et al. 2017, 2020; Adhikari et al. 2022), leading to different cascade rates in directions perpendicular and parallel to the mean magnetic field (MacBride et al. 2008; Andrés et al. 2022). Here, perpendicular means that the flow direction is perpendicular to the mean magnetic field, and parallel means that the flow is aligned with the mean magnetic field. Anisotropy can be studied via (i) spectral anisotropy (Horbury et al. 2008; Podesta 2009; Zhao et al. 2022a); (ii) variance anisotropy (Montgomery 1982; Matthaeus et al. 1990; Bieber et al. 1996), and (iii) correlation anisotropy (Dasso et al. 2005; Matthaeus et al. 2005; Wang et al. 2019; Bandyopadhyay & McComas 2021). The variance anisotropy is calculated by the relative magnitude of the fluctuations in directions parallel and perpendicular to the mean magnetic field, while the spectral anisotropy is determined relative to the direction of  $\mathbf{k}$ . Therefore, they are unique and there is no dependency between them (Matthaeus et al. 1996; Oughton et al. 2015).

MacBride et al. (2008) calculated perpendicular and parallel turbulent cascade rates, and isotropic turbulence cascade rate from Advanced Composition Explorer–Solar Wind Electron Proton Alpha Monitor (ACE–SWEPAM) magnetometer and plasma data sets (see also Smith & Vasquez 2021). They found that the perpendicular turbulent cascade rate is larger than the

parallel turbulence cascade rate. Recently, Andrés et al. (2022) studied the incompressible energy cascade rate in anisotropic solar wind turbulence using more than 2 yr of slow solar wind Parker Solar Probe (PSP) data sets (see their Section 3.2 entitled “The 2D and slab energy cascade rates MacBride et al. 2008.”) Andrés et al. (2022) present the cascade rate in perpendicular and parallel geometries 2D and slab cascade rates, respectively. Adhikari et al. (2020a) calculated the theoretical 2D and nearly incompressible (NI)/slab (hereafter called slab) turbulent cascade rates from the base of the solar corona to  $100 R_{\odot}$  (where  $R_{\odot} (= 6.95 \times 10^5 \text{ km})$  is the solar radius) using a NI MHD turbulence transport theory (Zank et al. 2017). They found that the turbulent cascade rate corresponding to 2D turbulence is larger than that of slab turbulence.

In this manuscript, we study the radial evolution of the 2D and slab turbulent cascade rates for the transverse total turbulent energy, transverse cross helicity, transverse outward and inward Elsässer energies, transverse fluctuating magnetic energy density, and transverse fluctuating kinetic energy theoretically and observationally as a function of heliocentric distance. We use the slow solar wind data sets from the first orbit PSP and Solar Orbiter (SolO) measurements, NI MHD turbulence transport theory (Zank et al. 2017), and the Adhikari et al. (2021a, 2022) approach. Adhikari et al. (2022) developed a method to calculate the transverse turbulence energy and the transverse correlation length relative to the mean magnetic field direction. Adhikari et al. (2021a) used dimensional analysis to calculate the turbulence cascade rate between the power spectrum in the energy-containing range and the power spectrum in the inertial range (Adhikari et al. 2017b).

We determine the 2D and slab cascade rates from the transverse cascade rate according to the criteria, (i)  $65^\circ < \theta_{\text{UB}} < 115^\circ$  and (ii)  $0^\circ < \theta_{\text{UB}} < 25^\circ$  (or  $155^\circ < \theta_{\text{UB}} < 180^\circ$ ), respectively, where  $\theta_{\text{UB}}$  is the angle between the mean magnetic field and the mean solar wind speed. The cascade rate in a perpendicular geometry (i.e., criterion i) is the 2D cascade rate, and that in the parallel geometry (i.e., criterion ii) is the slab cascade rate. Our method is close to the method of Bieber et al. (1996; see also Zank et al. 2020). Equation (18) of Bieber et al. (1996) is the total power spectrum, which is the sum of slab and 2D power spectra (the first and second terms on the right-hand side of Equation (18), respectively). Bieber et al. show that as the field angle  $\psi$  increases, the slab contribution to the frequency spectrum decreases in proportion to  $\cos \psi^{(q-1)}$ , while the 2D contribution increases proportionally to  $\sin \psi^{(q-1)}$ , where  $q$  is the power-law exponent. Obviously, when the field angle approaches  $0^\circ$ , the 2D contribution is almost negligible, and the measured turbulence energy is equivalent to the slab turbulence energy. Similarly, when the field angle is close to  $90^\circ$ , the slab contribution is about zero, and the measured turbulence energy is equivalent to the 2D turbulence energy.

Zank et al. (2022) reported that PSP observed only the slab turbulence component in the sub- and super-Alfvénic regions during encounter 8 near perihelion based on  $\theta_{\text{UB}}$  values of  $15^\circ$  and  $18^\circ$ , respectively (see also Telloni et al. 2019; Zhao et al. 2020; Zank et al. 2020). In addition, Zank et al. (2022) argued that the density fluctuations are advected by the dominant 2D velocity fluctuations in the region, despite PSP only measuring the slab component. Recently, Adhikari et al. (2022) used the 2D+slab model and (i) and (ii) to find reasonable agreement

between the observed and theoretical (Zank et al. 2017) 2D and slab results.

The 2D+slab model (e.g., Matthaeus et al. 1990) is an idealized model, which does not make any inherent assumptions about the specific properties of the waves, but only the wavevector dependence of each segment. In other words, Alfvén waves and 2D turbulence are good candidates for slab and 2D components, respectively. Although 2D+slab models are not more realistic than the phenomenology based on critical balance (CB) theory (Goldreich & Sridhar 1995), these models successfully describe much of the observed properties of turbulence (Zank et al. 2017, 2018b, 2021; Adhikari et al. 2017a, 2020b, 2020a).

The paper is structured as follows. We discuss the theory of turbulent cascade rate in Section 2. The data analysis is discussed in Section 3. Section 4 investigates the transverse cascade rate as a function of  $\theta_{\text{UB}}$ . Section 5 presents the comparison results between the theory and observations. We summarize this work in Section 6. The Appendix presents the Solar wind + NI MHD turbulence transport model equations.

## 2. Turbulent Transport Theory: Turbulent Cascade Rate

In turbulence transport theory, the nonlinear term transfers turbulent (kinetic + magnetic) energy from large scales to small scales and is then dissipated as heat energy. In deriving the turbulence transport model equation, the implicit assumption is that the energy input rate in the inertial range is equal to the energy dissipation rate in the dissipation range. During this process, the energy transfer rate follows a certain type of power law in the form of Kolmogorov (Batchelor 1953; Zank et al. 1996; Breech et al. 2008; Zank et al. 2012, 2017) or Iroshnikov–Kraichnan (IK; Iroshnikov 1964; Ng et al. 2010). The turbulence transport model equations describe the evolution of the energy-containing range fluctuations. The decay of these fluctuations occurs in the dissipation range, which terminates the energy cascade through the inertial range. Strictly speaking, the nonlinear term of the turbulence transport model equations calculates the rate at which energy enters the inertial range, and which is eventually dissipated as heat energy.

We present the NI MHD turbulence transport model equations in the Appendix. Here, we discuss the turbulence cascade rate from the perspective of NI MHD turbulence transport theory. The turbulent cascade rate corresponding to the 2D outward and inward Elsässer energies  $\langle z^{\infty \pm 2} \rangle$ , and the decay rate of the 2D residual energy  $E_D^\infty$  are given by Zank et al. (2017)

$$\begin{aligned} \epsilon_{\langle z^{\infty \pm 2} \rangle} &= 2\alpha \frac{\langle z^{\infty \pm 2} \rangle \langle z^{\infty \mp 2} \rangle^{1/2}}{\lambda_\infty^\pm}; \\ \Gamma_{E_D}^\infty &= \alpha E_D^\infty \left( \frac{\langle z^{\infty -2} \rangle^{1/2}}{\lambda_\infty^+} + \frac{\langle z^{\infty +2} \rangle^{1/2}}{\lambda_\infty^-} \right), \end{aligned} \quad (1)$$

where  $\lambda_\infty^\pm$  are the corresponding correlation lengths, and  $\alpha$  ( $= 0.02$ ) is the von Kármán–Taylor constant. Similarly, the turbulent cascade rates corresponding to the slab outward and inward Elsässer energies  $\langle z^{* \pm 2} \rangle$ , and the decay rate of the slab

residual energy  $E_D^*$  are given by,

$$\begin{aligned} \epsilon_{\langle z^{\pm 2} \rangle}^* &= 2\alpha \frac{\langle z^{\pm 2} \rangle \langle z^{\infty \mp 2} \rangle^{1/2}}{\lambda_{\infty}^{\pm}}; \\ \Gamma_{E_D}^* &= \alpha E_D^* \left( \frac{\langle z^{\infty - 2} \rangle^{1/2}}{\lambda_{\infty}^+} + \frac{\langle z^{\infty + 2} \rangle^{1/2}}{\lambda_{\infty}^-} \right). \end{aligned} \quad (2)$$

Equation (2) shows that the minority slab turbulence (“\*”) interacts with the majority 2D turbulence (“ $\infty$ ”) in a passive scalar sense, so that the transfer rate of the minority slab turbulence energy is due to mixing rather than nonlinearity as in Equation (1). The 2D turbulent cascade rate (with an analogous definition for slab component) corresponding to the total turbulent energy  $E_T$  and the cross helicity  $E_c$  can be written as,

$$\epsilon_{E_T}^{\infty} = \frac{\epsilon_{\langle z^{+2} \rangle}^{\infty} + \epsilon_{\langle z^{-2} \rangle}^{\infty}}{2}; \quad \epsilon_{E_c}^{\infty} = \frac{\epsilon_{\langle z^{+2} \rangle}^{\infty} - \epsilon_{\langle z^{-2} \rangle}^{\infty}}{2}. \quad (3)$$

Similarly, the 2D turbulent cascade rate (with corresponding definitions for slab turbulence) for the turbulent kinetic energy Bieber et al. (1996)  $\langle u^2 \rangle$  and the turbulent magnetic energy density  $E_b$  can be written as (Adhikari et al. 2021a)

$$\begin{aligned} \epsilon_{\langle u^2 \rangle}^{\infty} &= \frac{\epsilon_{\langle z^{+2} \rangle}^{\infty} + \epsilon_{\langle z^{-2} \rangle}^{\infty} + 2\Gamma_{E_D}^{\infty}}{4}; \\ \epsilon_{E_b}^{\infty} &= \frac{\epsilon_{\langle z^{+2} \rangle}^{\infty} + \epsilon_{\langle z^{-2} \rangle}^{\infty} - 2\Gamma_{E_D}^{\infty}}{4}. \end{aligned} \quad (4)$$

We note that the fluctuating kinetic energy and magnetic energy density cascade rates are not physically verified, as well as the decay rate of the residual energy. The MHD range values of the 2D and slab turbulence energy and the corresponding 2D and slab correlation lengths are required to calculate the turbulence cascade rates, which were obtained in Adhikari et al. (2022) and reproduced in Figure 1. The theoretical results of Adhikari et al. (2022) are obtained from solving the Solar Wind + NI MHD turbulence transport model equations (see the Appendix) using PSP measurements for the boundary conditions for slab turbulence and prescribing the 2D boundary conditions in such a way that the theoretical solutions are similar to the PSP and SolO measurements. Figure 1 compares the theoretical and observed 2D and slab turbulence energy and correlation lengths as a function of distance. Figures 1(a)–(g) show the total turbulence energy, the normalized cross helicity, the normalized residual energy, the outward Elsässer energy, the inward Elsässer energy, the correlation length corresponding to outward Elsässer energy, and the correlation length corresponding to inward Elsässer energy as a function of distance, respectively. In the figure, the red and blue curves denote the theoretical 2D and slab components. The red and cyan scatter plots denote the observed 2D component measured by PSP and SolO. The blue and black scatter plots denote the observed slab component measured by PSP and SolO. Clearly, the 2D turbulence energy is larger than the slab turbulence energy, and the slab correlation length is larger than the 2D correlation length as a function of distance (see Adhikari et al. 2022, for details).

We compare the theoretical 2D, slab, and 2D+slab cascade rates with the observed 2D and slab, and total (the case in which no distinction is made between 2D and slab turbulence cascade rates) transverse cascade rates measured by PSP; Solar Wind Electrons Alphas & Protons (SWEAP; Kasper et al. 2016) and FIELDS (Bale et al. 2016), and Solar Orbiter (SolO); magnetometer (Horbury et al. 2020) and Solar Wind Analyser; and Proton and Alpha Sensor (SWA–PAS) plasma (Owen et al. 2020).

### 3. Data Analysis

We first use the method of Adhikari et al. (2022) to calculate the transverse (T) turbulence energy and transverse correlation length. A fluctuating vector  $\mathbf{a}$  ( $=a_r \hat{r} + a_t \hat{t} + a_n \hat{n}$ , where  $a_r$ ,  $a_t$ , and  $a_n$  are the  $R$ ,  $T$ , and  $N$  components of a vector  $\mathbf{a}$ ) can be decomposed into parallel and perpendicular vectors relative to the mean magnetic field  $\mathbf{B}$  as

$$\mathbf{a} = \mathbf{a}_{\parallel} + \mathbf{a}_{\perp} = a_{\parallel} \hat{b} + \mathbf{a}_{\perp}.$$

where  $\hat{b} = \mathbf{B}/|\mathbf{B}|$  is the unit vector,  $|\mathbf{B}|$  is the magnitude of the mean magnetic field of the intervals (e.g., a 3 hr long interval), and  $\mathbf{a}_{\perp}$  and  $\mathbf{a}_{\parallel}$  ( $=a_{\parallel} \hat{b}$ ) are the perpendicular and parallel vectors, respectively. The perpendicular vector  $\mathbf{a}_{\perp}$  can be expressed in  $R$ ,  $T$ , and  $N$  coordinates as (Adhikari et al. 2022)

$$\begin{aligned} \mathbf{a}_{\perp} &= \frac{C_T B_N - C_N B_T}{|\mathbf{B}|^2} \hat{r} + \frac{C_N B_R - C_R B_N}{|\mathbf{B}|^2} \hat{t} \\ &+ \frac{C_R B_T - C_T B_R}{|\mathbf{B}|^2} \hat{n}, \end{aligned} \quad (5)$$

where  $C_R = B_T a_n - B_N a_t$ ,  $C_T = B_N a_r - B_R a_n$ ,  $C_N = B_R a_t - B_T a_r$ , and  $|\mathbf{B}|^2 (=B_R^2 + B_T^2 + B_N^2)$  is the square of the magnitude of the mean magnetic field. The parameters  $B_R$ ,  $B_T$ , and  $B_N$  are the  $R$ ,  $T$ , and  $N$  components of the mean magnetic field. Using the  $R$ ,  $T$ , and  $N$  components of the perpendicular vector, we calculate the transverse outward and inward Elsässer energies  $\langle z_{\mp}^{\pm 2} \rangle$ , transverse fluctuating magnetic energy density  $E_b^T$ , transverse fluctuating kinetic energy  $\langle u_T^2 \rangle$ , and the corresponding transverse correlation lengths (Zank et al. 1996; Adhikari et al. 2015, 2022). Then, we calculate the transverse turbulent cascade rate for the  $E_b^T$ ,  $\langle z_{\mp}^{\pm 2} \rangle$ , and  $\langle u_T^2 \rangle$  using the equations (Adhikari et al. 2021a),

$$\begin{aligned} \epsilon_{E_b^T}^T &= \frac{(E_b^T)^{3/2}}{\left[ C_K \log \left( \frac{1}{k_{\text{inj}} \lambda_T^b} \right) \right]^{3/2} \lambda_T^b}; \\ \epsilon_{\langle z^{\pm 2} \rangle}^T &= \frac{\langle z_{\mp}^{\pm 2} \rangle^{3/2}}{\left[ C_K \log \left( \frac{1}{k_{\text{inj}} \lambda_T^{\pm}} \right) \right]^{3/2} \lambda_T^{\pm}}; \\ \epsilon_{\langle u^2 \rangle}^T &= \frac{\langle u_T^2 \rangle^{3/2}}{\left[ C_K \log \left( \frac{1}{k_{\text{inj}} \lambda_T^u} \right) \right]^{3/2} \lambda_T^u}, \end{aligned} \quad (6)$$

respectively, where  $\lambda_T^b$  is the transverse correlation length of  $E_b^T$ ,  $\lambda_T^{\pm}$  the transverse correlation length corresponding to  $\langle z_{\mp}^{\pm 2} \rangle$ , and  $\lambda_T^u$  the transverse correlation length of  $\langle u_T^2 \rangle$ . The parameter  $C_K = 1.6$  is the Kolmogorov constant (Yeung & Zhou 1997), and the injection wavenumber  $k_{\text{inj}} \sim 1.07 \times 10^{-9} \text{ km}^{-1}$  is

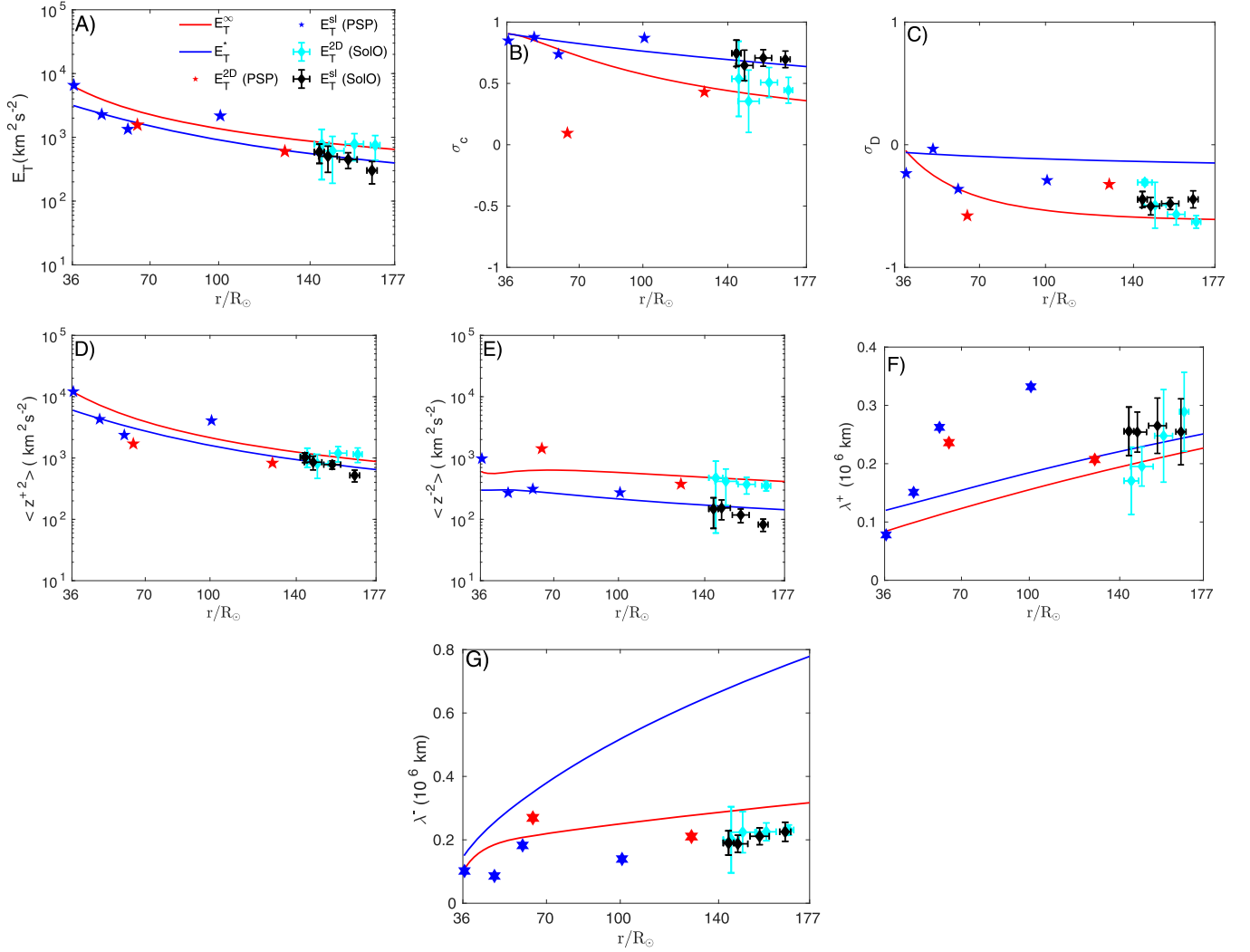


**Figure 1.** Comparison between the theoretical and observed 2D and slab total turbulent energy (a), normalized cross helicity (b), normalized residual energy (c), outward and inward Elsässer energies (d) and (e), and the correlation lengths corresponding to outward and inward Elsässer energies (f) and (g) as a function of heliocentric distance. The solid red curve, and red and cyan scatter plots denote the theoretical and observed 2D component. The solid blue curve, and blue and black scatter plots denote the theoretical and observed slab component (reproduced from Adhikari et al. 2022).

equivalent to one solar rotation  $\sim 27$  days (Adhikari et al. 2017b). Similarly, the transverse turbulent cascade rates for the total transverse turbulent energy  $E_T^T$ , and the transverse cross helicity  $E_c^T$  are given by,

$$\epsilon_{E_T}^T = \frac{\epsilon_{(z^+)}^T + \epsilon_{(z^-)}^T}{2}; \quad \epsilon_{E_c}^T = \frac{\epsilon_{(z^+)}^T - \epsilon_{(z^-)}^T}{2}. \quad (7)$$

Using Equations (6) and (7) we calculate the observed transverse turbulence cascade rates using the values of the transverse turbulence quantities calculated in a 3 hr long intervals, where we also calculate the angle between the mean magnetic field and mean solar wind speed  $\theta_{UB}$ . To compare with the theoretical 2D and slab turbulence cascade rates derived from NI MHD turbulence transport theory (Zank et al. 2017), we calculate the observed slab and 2D turbulence cascade rates based on two criteria, i)  $0^\circ < \theta_{UB} < 25^\circ$  (or  $155^\circ < \theta_{UB} < 180^\circ$ ), and ii)  $65^\circ < \theta_{UB} < 115^\circ$ . For other angles  $\theta_{UB}$ , there can be a mixture of 2D and slab turbulence. One can decompose it into 2D and slab components separately. However, this is not the focus of this work.

#### 4. Turbulence Cascade Rate versus $\theta_{UB}$

We discuss the transverse turbulence cascade rate as a function of  $\theta_{UB}$ . We select 1 day long data sets from PSP at a distance  $\sim 66.3 R_\odot$ , and from SolO at  $\sim 176.3 R_\odot$ . We calculate the angle between the mean magnetic field and mean solar wind speed, and the various transverse cascade rates in 3 hr long moving intervals. Figure 2(a) shows the histogram of  $\theta_{UB}$  during the period 2018 November 13 (or DOY 317) from PSP measurements. Here  $\theta_{UB}$  varies between  $27^\circ$  and  $100^\circ$ , and we only consider the results until  $\theta_{UB} = 100^\circ$ . Note that in this particular period or distance, PSP does not observe slab fluctuations, but observes 2D fluctuations. Figures 2(b), (c), (d), (e), (f), and (g) show the transverse turbulent cascade rates  $\epsilon_{E_T}^T$ ,  $\epsilon_{E_c}^T$ ,  $\epsilon_{(z^+)}^T$ ,  $\epsilon_{(z^-)}^T$ ,  $\epsilon_{E_B}^T$ , and  $\epsilon_{(u^2)}^T$ , respectively as a function of  $\theta_{UB}$ . Dots denote all the transverse turbulent cascade rates, while filled circles denote the binned transverse turbulent cascade rates over a  $10^\circ$  width. The averaged  $\epsilon_{E_T}^T$  at  $\theta_{UB} = 31.21^\circ$  is  $\sim 5 \times 10^3 \text{ Joule kg}^{-1} \text{ s}^{-1}$ , which decreases initially and then increases as  $\theta_{UB}$  increases, and reaches  $\sim 2 \times 10^4 \text{ Joule kg}^{-1} \text{ s}^{-1}$  at  $\theta_{UB} \sim 98^\circ$ . Similarly, the  $\epsilon_{E_c}^T$  at  $\theta_{UB} = 31.21^\circ$  is  $\sim 4 \times 10^3 \text{ Joule kg}^{-1} \text{ s}^{-1}$ , which also shows

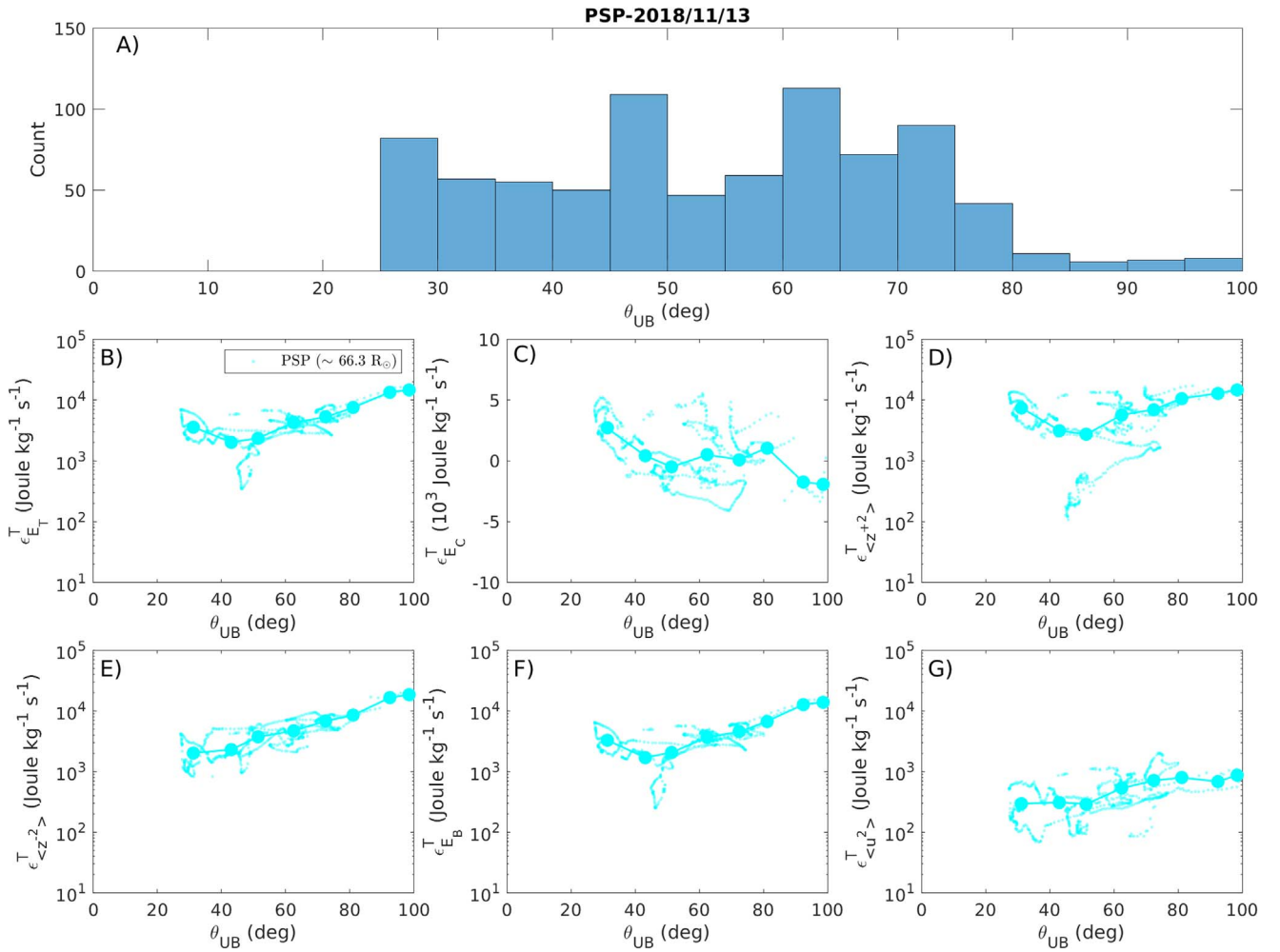


**Figure 2.** (a) Histogram of the angle between the mean solar wind speed and mean magnetic field ( $\theta_{UB}$ ) during the period 2018 November 13 (or DOY 317) measured by PSP at  $\sim 66.3 R_{\odot}$ . The transverse turbulent cascade rate of the transverse total turbulent energy (b), transverse cross helicity (c), transverse energy in backward propagating modes (d), transverse fluctuating magnetic energy density (e), and transverse fluctuating kinetic energy (f), and transverse fluctuating magnetic energy density (g) is shown as a function of  $\theta_{UB}$ . Dots denote all the transverse turbulent cascade rates, and filled circles denote the binned transverse turbulent cascade rates over a  $10^{\circ}$  width.

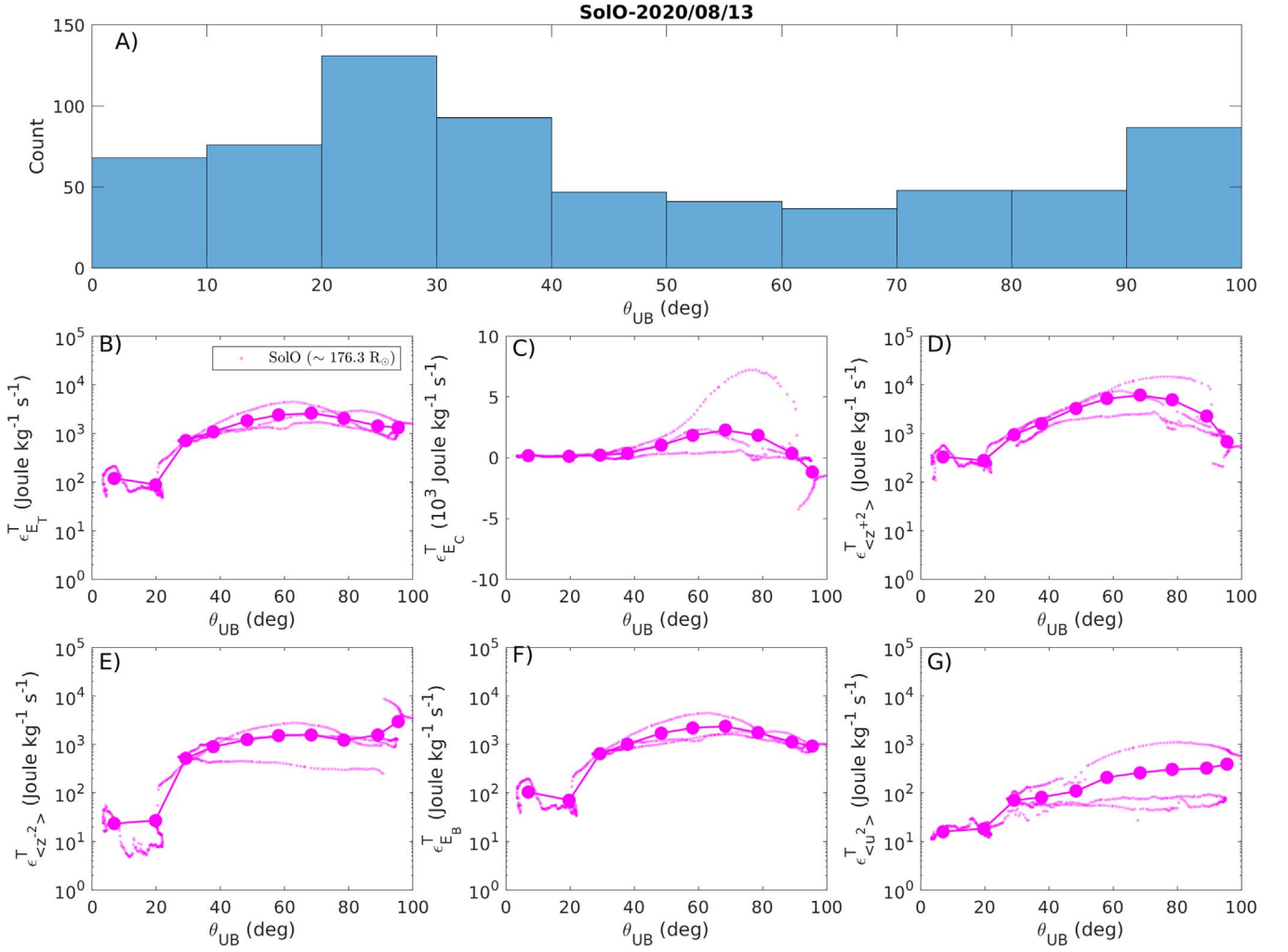
the negative values between  $\theta_{UB} \sim 36^{\circ}$ – $70^{\circ}$ , followed by a slow increase, and then decreases toward the negative value. The negative  $\epsilon_{E_C}^T$  between  $\theta_{UB} \sim 36^{\circ}$ – $70^{\circ}$  is due to the smaller  $\epsilon_{(z^+z^-)}^T$  than the  $\epsilon_{(z^-z^+)}^T$  (Figures 2(d) and (e)). The  $\epsilon_{(z^+z^-)}^T$  shows a dip between  $\theta_{UB} \sim 31^{\circ}$ – $70^{\circ}$ , and then a slight increase. The  $\epsilon_{(z^-z^+)}^T$  increases gradually as a function of  $\theta_{UB}$ . The  $\epsilon_{E_B}^T$  and  $\epsilon_{(u^2)}^T$  also increase with increasing  $\theta_{UB}$ , in which the prior is larger than the latter, indicating that the heating rate corresponding to magnetic field fluctuations is larger than that corresponding to the velocity fluctuations.

Figure 3(a) shows a histogram of  $\theta_{UB}$  during the period 2020 August 13 from SolO measurements at  $\sim 176.3 R_{\odot}$ . The angle  $\theta_{UB}$  varies between  $3^{\circ}$ – $100^{\circ}$ , indicating that SolO observes both slab and 2D components. In Figures 3(b)–(g), dots denote all the transverse turbulent cascade rates, while filled circles denote the binned transverse turbulent cascade rates over a  $10^{\circ}$  width. Corresponding to Figures 3(b)–(g), various transverse turbulence cascade rates clearly show that the turbulent cascade rate near  $\theta_{UB} = 90^{\circ}$  (where only 2D fluctuations can be observed) is larger than that near  $\theta_{UB} = 10^{\circ}$  (where only slab fluctuations can be observed). Consequently, the 2D heating rate is observed to be larger than the slab

heating rate at  $176.3 R_{\odot}$ , consistent with that found by Andrés et al. (2022; see also Oughton & Matthaeus 2005; MacBride et al. 2008). The binned  $\epsilon_{E_C}^T$  increases slightly until  $\theta_{UB} = 68^{\circ}$ , and decreases toward negative values.

## 5. Radial Evolution of 2D and Slab Turbulence Cascade Rates

For the slow wind at PSP, we use the SWEAP and FIELDS data sets at times (DOY:HR:MIN): 309:3:18–311:12:44, 313:9:29–314:3:20, 315:16:52–317:22:59, 324:22:51–325:13:19, 332:7:52–333:23:57 of year 2018 (see Adhikari et al. 2020b). For the slow wind of SolO, we use the magnetometer and plasma data sets at times (YY:MN:DD): 2020 July 17, 2020 July 18, 2020 July 22, 2020 July 30, 2020 September 2, 2020 September 3, 2020 September 4, 2020 September 5, 2020 September 7, 2020 September 8, 2020 September 9, 2020 September 11, 2020 September 13 (see Adhikari et al. 2021c). During this period, SolO covers a heliocentric distance  $\sim 142$ – $177 R_{\odot}$  and stays within a latitude of  $5^{\circ}$ , indicating that SolO observes the same kind of plasma in which the speed ranges from  $\sim 335$ – $360 \text{ km s}^{-1}$  (Adhikari et al. 2021c). Similarly, PSP also stays within a latitude of  $5^{\circ}$  from



**Figure 3.** (a) Histogram of the angle between the mean solar wind speed and mean magnetic field ( $\theta_{UB}$ ) during the period 2020 August 13 measured by SoLo at  $\sim 176.3 R_{\odot}$ . The format of the figure is similar to Figure 1.

$\sim 309$  to  $334$  DOY of 2018, and covers a distance  $\sim 36.67$ – $129 R_{\odot}$ . The solar wind speed measured by PSP ranges from  $\sim 332$ – $353 \text{ km s}^{-1}$  over the distance  $\sim 36.67$ – $55 R_{\odot}$ , and  $380$ – $392 \text{ km s}^{-1}$  from  $\sim 100$  to  $129 R_{\odot}$  (Adhikari et al. 2021c). This indicates that PSP and SoLo observe a similar type of slow solar wind despite not being the same plasma parcel. The PSP data intervals vary from  $\sim 1$  day to  $\sim 2$  days, while SoLo data intervals are 1 day long. In each  $\sim 1$  day or  $\sim 2$  days long interval, we calculate the angle between the mean magnetic field and the mean solar wind speed, transverse outward and inward Elsässer energies, transverse fluctuating magnetic energy density, transverse fluctuating kinetic energy, and the corresponding transverse correlation lengths using 3 hr long moving intervals. We calculate various transverse turbulent cascade rates from the transverse turbulence components, and then determine the slab and 2D cascade rates using criteria (i) and (ii).

Figure 4 compares the theoretical and observed turbulent cascade rates as a function of heliocentric distance. The solid black curve is the theoretical 2D turbulent cascade rate, the dashed black curve is the theoretical slab turbulent cascade rate, and the dashed–dotted–dashed black curve is the theoretical 2D +slab turbulent cascade rate. Green stars denote total observed transverse turbulent cascade rates, and red and blue dots the

observed turbulent cascade rates determined by the  $\theta_{UB}$  criteria (i) and (ii), respectively. Hence, we may regard the red and blue dots as the observed 2D and slab turbulent cascade rates. From perihelion ( $\sim 36.66 R_{\odot}$ ) to  $65 R_{\odot}$ , PSP measures mainly the slab (and not the 2D) turbulent cascade rates because the background fields are almost parallel or antiparallel. However, PSP and SoLo observe both the 2D and slab cascade rates between  $65$  and  $177 R_{\odot}$ . In Figure 4(a), the observed  $\epsilon_{E_T}^{sl}$  is about  $10^5 \text{ Joule kg}^{-1} \text{ s}^{-1}$  near perihelion, and is similar to the theoretical  $\epsilon_{E_T}^*$ . Then, the observed  $\epsilon_{E_T}^{sl}$  decreases more rapidly than the theoretical  $\epsilon_{E_T}^*$ . Similarly, the observed  $\epsilon_{E_T}^{2D}$  is about  $10^4 \text{ Joule kg}^{-1} \text{ s}^{-1}$  at  $\sim 66 R_{\odot}$ , which decreases monotonically with distance. The theoretical  $\epsilon_{E_T}^*$  is larger than the PSP measurement, but is similar to the SoLo observed value. The theoretical result shows that the 2D cascade rate is larger than the slab cascade rate between  $36.66$  and  $177 R_{\odot}$ . The observed result shows the greater strength of the 2D cascade rate between  $65$  and  $177 R_{\odot}$ . Similarly, the theoretical 2D+slab and the total observed transverse total turbulence energy cascade rate decrease with increasing distance. Both the theoretical and observed results show that the 2D cascade rate is larger than the slab cascade rate. Compared to the red and blue dots, the green stars show a large scatter.

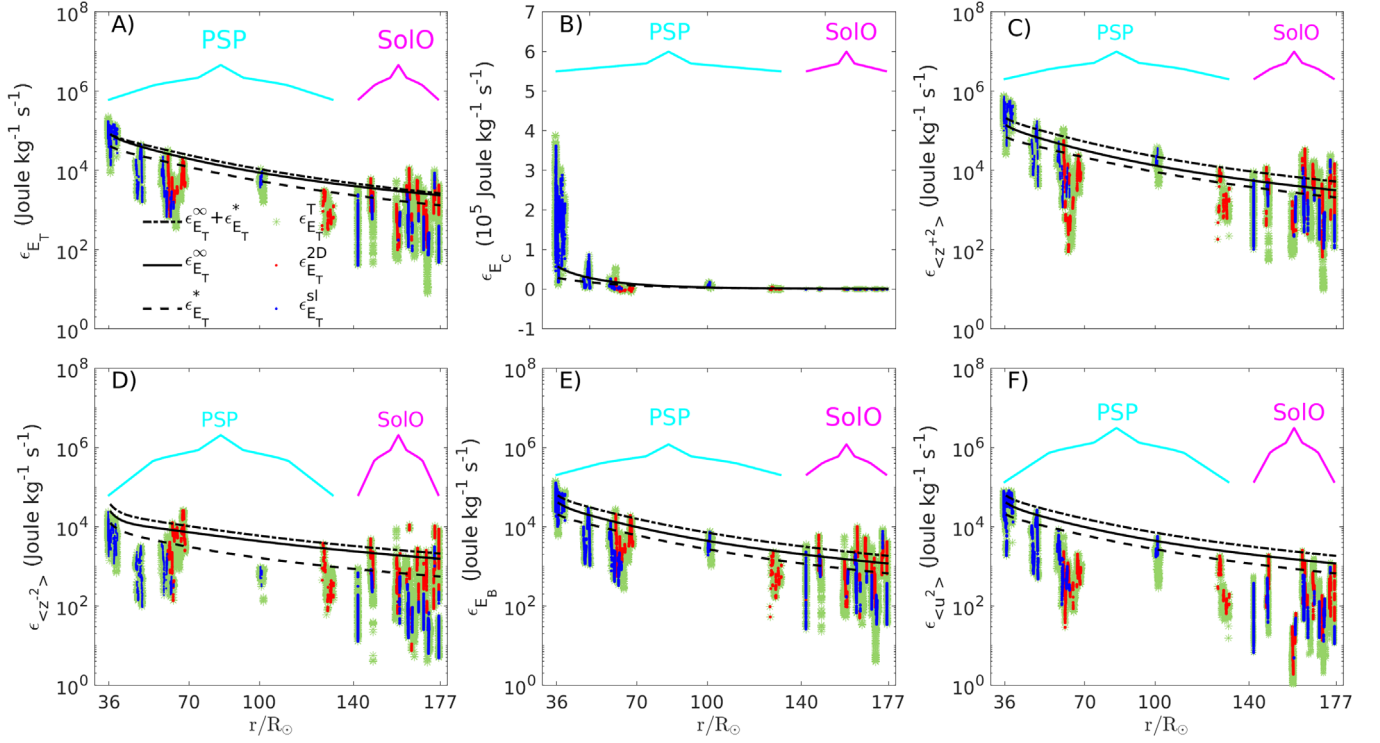


**Figure 4.** Comparison between the theoretical (2D, slab, and 2D+slab), and observed (2D, slab, and total transverse) turbulent cascade rates of the total turbulence energy (a), cross helicity (b), outward Elsässer energy (c), inward Elsässer energy (d), fluctuating magnetic energy density (e), and fluctuating kinetic energy (f) as a function of heliocentric distance. The solid black curve is the theoretical 2D turbulent cascade rate, the dashed black curve is the theoretical slab turbulent cascade rate, and the dashed–dotted–dashed is the theoretical 2D+slab turbulent cascade rate. Green stars denote total observed transverse turbulent cascade rates, red dots the observed 2D turbulent cascade rate, and blue dots the observed slab turbulent cascade rate.

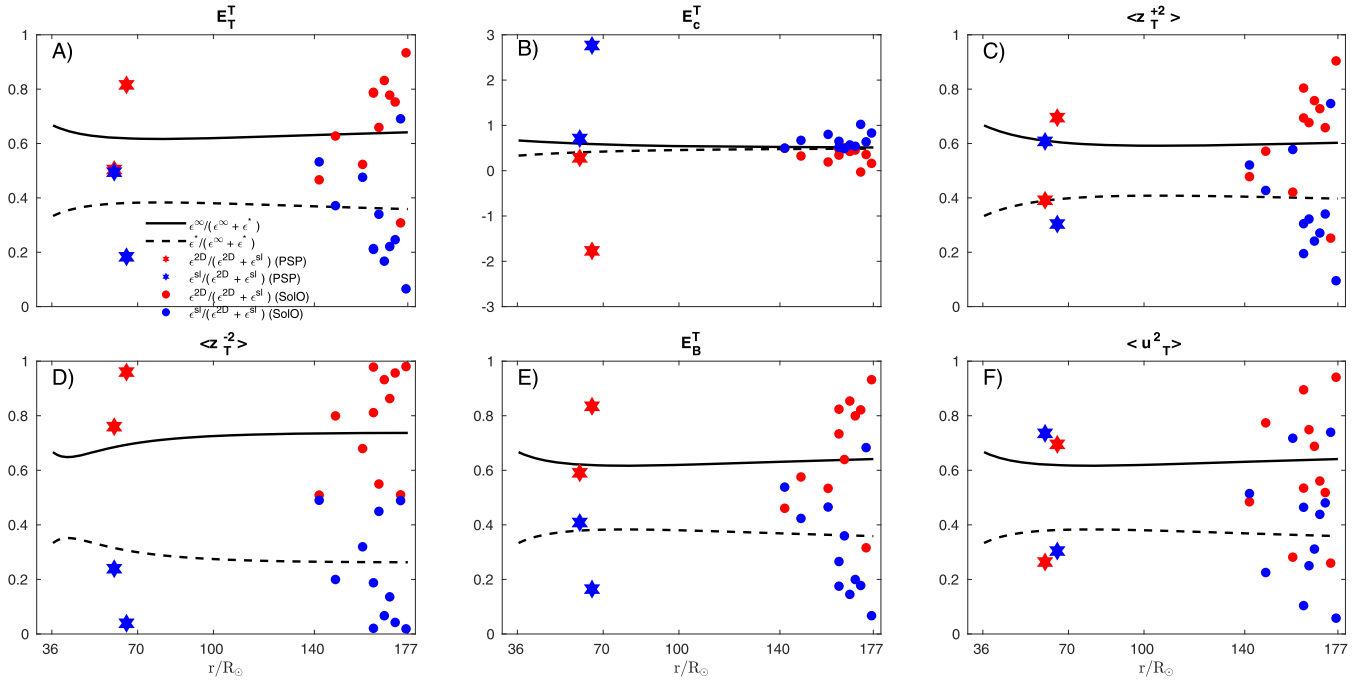
Figure 4(b) illustrates the transverse cross-helicity cascade rate  $\epsilon_{E_C}^T$  (which is the difference between the transverse outward and inward Elsässer energy heating rates). Near perihelion, the mean value of the observed slab (blue dots) and total observed transverse (green stars) cross-helicity cascade rate is  $\sim 2 \times 10^5$  Joule  $\text{kg}^{-1}\text{s}^{-1}$ . This means that the outward Elsässer energy is more important to heat the solar wind near the Sun. The observed slab, 2D, and total transverse  $\epsilon_{E_C}^T$  are small beyond  $\sim 50 R_\odot$ , which means that the inward Elsässer energy can also be an important factor to heat the solar wind at large distances. The theoretical  $\epsilon_{E_C}^\infty$  is larger than the theoretical  $\epsilon_{E_C}^*$  from  $\sim 36.66$ – $50 R_\odot$ , and then both the theoretical results are approximately similar. Although, the observed results are larger than the theoretical results below  $50 R_\odot$ , both the theoretical and observed results are similar beyond  $50 R_\odot$ .

Figure 4(c) shows that the observed  $\epsilon_{\langle z^+2 \rangle}^{sl}$  is  $\sim 3 \times 10^5$  Joule  $\text{kg}^{-1}\text{s}^{-1}$  near perihelion. The  $\epsilon_{\langle z^+2 \rangle}^{sl}$  decreases in a similar fashion to that of the theoretical  $\epsilon_{\langle z^+2 \rangle}^*$  until  $\sim 165 R_\odot$ , and then the observed result decreases more rapidly than the theoretical result. The observed  $\epsilon_{\langle z^+2 \rangle}^{sl}$  is about  $\sim 2 \times 10^4$  Joule  $\text{kg}^{-1}\text{s}^{-1}$  at  $65 R_\odot$ , and decreases as a function of distance. The theoretical  $\epsilon_{\langle z^+2 \rangle}^\infty$  is consistent with the SoLo measurements, and is in reasonable agreement with the PSP measurements. The theoretical 2D+slab turbulence cascade rate and total observed turbulence cascade rate (green stars) also decrease as a function of distance. In the figure, red and blue dots are less scattered, while green stars show a larger variation. Theoretically, the 2D cascade rate is larger than the slab cascade rate from  $\sim 36.66$ – $177 R_\odot$ , which is confirmed by SoLo measurements between  $\sim 140$ – $177 R_\odot$ . But PSP measurement does not

show clearly that the observed  $\epsilon_{\langle z^+2 \rangle}^{2D}$  is larger than the observed  $\epsilon_{\langle z^+2 \rangle}^{sl}$ . However, the theoretical and SoLo observed results indicate that the 2D heating rate is larger than the slab heating rate.

In Figure 4(d), we show the theoretical and observed transverse cascade rate of the inward Elsässer energy. Similar to the previous results, the theoretical and observed 2D cascade rates are larger than the corresponding slab cascade rates. The theoretical  $\epsilon_{\langle z^-2 \rangle}^\infty$  shows good agreement with the observed  $\epsilon_{\langle z^-2 \rangle}^{2D}$ . The theoretical  $\epsilon_{\langle z^-2 \rangle}^*$  is similar to the observed result near perihelion, but is larger than the observed with increasing distance. The theoretical 2D+slab cascade rate and total observed transverse cascade rate (green stars) for  $\langle z_T^{-2} \rangle$  decrease gradually with distance, where the green stars show a large scatter.

We also study the turbulence cascade rate for the fluctuating magnetic energy density (Figure 4(e)) and the fluctuating kinetic energy (Figure 4(f)). Theoretically and observationally, the 2D turbulent magnetic energy density cascade rate is predominantly larger than the slab magnetic cascade rate, and both decrease as a function of distance. The theoretical 2D+slab  $\epsilon_{E_B}$  is consistent with total observed transverse magnetic cascade rates (green stars). Similarly, the theoretical and observed 2D cascade rates for the fluctuating kinetic energy are larger than the corresponding slab cascade rates. The theoretical  $\epsilon_{\langle u^2 \rangle}^*$  is consistent with the observed  $\epsilon_{\langle u^2 \rangle}^{sl}$  near perihelion, but larger than observed with increasing distance. The theoretical  $\epsilon_{\langle u^2 \rangle}^\infty$  is larger than the observed  $\epsilon_{\langle u^2 \rangle}^{2D}$  as a function of distance. Similarly, the theoretical 2D+slab  $\epsilon_{\langle u^2 \rangle}$  exceeds the observed  $\epsilon_{\langle u^2 \rangle}^T$  (green stars). The results show that the



**Figure 5.** Comparison of the theoretical and observed 2D and 2D+slab turbulence cascade rate (solid curve), and the slab and 2D+slab turbulence cascade rate (dashed curve) ratios as a function of heliocentric distance—correspond to Panels (a)–(e) of Figure 3. Red and blue circles are the ratios observed by SolO between the 2D and 2D+slab turbulence cascade rates, and the slab and 2D+slab turbulence cascade rates, respectively.

$\epsilon_{E_B}^T > \epsilon_{\langle u^2 \rangle}^T$  from  $36.66$ – $177 R_\odot$ , indicating that the heating rate corresponding to the magnetic field fluctuations is larger than that of the velocity fluctuations.

Figure 5 compares the theoretical and observed ratios of the 2D and 2D+slab, and the slab and 2D+slab turbulence cascade rates as a function of distance. In the figure, the solid curve (red circles) denote the theoretical (observed) ratio between the 2D and 2D+slab turbulent cascade rates, and the dashed curve (blue circles) the theoretical (observed) ratio between the slab and 2D+slab turbulent cascade rates. The observed ratio corresponds to the averaged values measured by PSP and SolO measurements over a 1 day long interval. In doing so, it is assumed that the solar wind plasma properties are the same within a 1 day interval. Figure 5(a) corresponds to the transverse total turbulent energy, in which the theoretical  $\epsilon_{E_T}^\infty / (\epsilon_{E_T}^\infty + \epsilon_{E_T}^*)$  lies between  $\sim 60\%$  and  $70\%$ , while the theoretical  $\epsilon_{E_T}^* / (\epsilon_{E_T}^\infty + \epsilon_{E_T}^*)$  lies between  $\sim 30\%$  and  $40\%$ . Despite the scatter of the  $\epsilon_{E_T}^{2D} / (\epsilon_{E_T}^{2D} + \epsilon_{E_T}^{sl})$ , the observed  $\epsilon_{E_T}^{2D} / (\epsilon_{E_T}^{2D} + \epsilon_{E_T}^{sl})$  is similar to the observed  $\epsilon_{E_T}^{sl} / (\epsilon_{E_T}^{2D} + \epsilon_{E_T}^{sl})$  near perihelion. However, the former is larger than the latter with increasing distance. The theoretical and observed results are in reasonable agreement. Figure 5(b) shows that the observed  $\epsilon_{E_c}^{2D} / (\epsilon_{E_c}^{2D} + \epsilon_{E_c}^{sl})$  is smaller than the observed  $\epsilon_{E_c}^{sl} / (\epsilon_{E_c}^{2D} + \epsilon_{E_c}^{sl})$  as a function of distance from  $36.66 R_\odot$  to  $177 R_\odot$ , whereas, the theoretical  $\epsilon_{E_c}^\infty / (\epsilon_{E_c}^\infty + \epsilon_{E_c}^*)$  is very marginally larger than the theoretical  $\epsilon_{E_c}^* / (\epsilon_{E_c}^\infty + \epsilon_{E_c}^*)$  and they converge to the same value by about  $100 R_\odot$ .

In Figure 5(c), the theoretical  $\epsilon_{\langle z^2 \rangle}^\infty / (\epsilon_{\langle z^2 \rangle}^\infty + \epsilon_{\langle z^2 \rangle}^*)$  is about  $65\%$  near perihelion, which initially decreases slightly, and then tends to  $60\%$  as a function of heliocentric distance, and agrees reasonably with the corresponding observed result. The theoretical  $\epsilon_{\langle z^2 \rangle}^* / (\epsilon_{\langle z^2 \rangle}^\infty + \epsilon_{\langle z^2 \rangle}^*)$  is about  $32\%$  at  $36.66 R_\odot$ , and  $40\%$  at  $177 R_\odot$ . Similarly, the theoretical  $\epsilon_{\langle z^{-2} \rangle}^\infty / (\epsilon_{\langle z^{-2} \rangle}^\infty + \epsilon_{\langle z^{-2} \rangle}^*)$

is also significantly larger than the theoretical  $\epsilon_{\langle z^{-2} \rangle}^* / (\epsilon_{\langle z^{-2} \rangle}^\infty + \epsilon_{\langle z^{-2} \rangle}^*)$  (Figure 5(d)), in which the prior lies between  $60\%$  and  $75\%$ , but lower than the PSP measurements and similar to the SolO measurements, whereas the latter lies between  $\sim 25\%$  and  $40\%$  and higher than the PSP measurements and similar to the SolO measurements.

Figure 5(e) also shows that the theoretical (and observed) ratio between the 2D and 2D+slab magnetic turbulence cascade rate is larger than the corresponding ratio between the slab and 2D+slab magnetic turbulence cascade rate as a function of distance. The theoretical and observed results are in reasonable agreement. Similar to the previous results, the theoretical (and observed) ratio between the 2D and 2D+slab turbulent kinetic energy cascade rate is also larger than the theoretical (and observed) ratio between the slab and 2D+slab turbulent kinetic energy cascade rate (Figure 5(f)).

## 6. Discussion and Conclusions

We studied the radial evolution of 2D and slab turbulence cascade rates theoretically and observationally from the perihelion of the first PSP orbit  $\sim 36.66 R_\odot$ – $177 R_\odot$  (using SolO data) in the slow solar wind. PSP and SolO stay within a latitude of  $5^\circ$  during the period of this study. Although the spacecraft are not radially aligned, they measure a similar type of slow solar wind. First, we calculated the transverse outward and inward Elsässer energy, transverse fluctuating magnetic energy density, transverse fluctuating kinetic energy, and the corresponding transverse correlation lengths using the method of Adhikari et al. (2022). Second, we used Adhikari et al. (2021a) to calculate the various observed transverse turbulence cascade rates. Finally, we used the angle between the mean magnetic field and mean solar wind speed  $\theta_{UB}$  to isolate the 2D and slab cascade rates (Bieber et al. 1996; Andrés et al. 2022), and compared the observed 2D, slab, and total transverse cascade rates with the theoretical 2D, slab, and 2D+slab

cascade rates. Specifically, we introduced the criteria, (i)  $65^\circ < \theta_{UB} < 115^\circ$  and (ii)  $0^\circ < \theta_{UB} < 25^\circ$  or  $155^\circ < \theta_{UB} < 180^\circ$ , where criterion (i) allows us to determine the 2D cascade rate, and criterion (ii) enables us to determine the slab cascade rate (Bieber et al. 1996; Adhikari et al. 2022; Andrés et al. 2022). In other words, the measured transverse heating rate corresponds to the slab cascade rate in for parallel geometry ( $0^\circ < \theta_{UB} < 25^\circ$  or  $155^\circ < \theta_{UB} < 180^\circ$ ), and corresponds to the 2D cascade rate for perpendicular geometry ( $65^\circ < \theta_{UB} < 115^\circ$ ) (e.g., Andrés et al. 2022) between the background fields. When  $\theta_{UB}$  approaches  $0^\circ$ , the 2D contribution is about zero, and the measured turbulence energy is equivalent to the slab turbulence. When  $\theta_{UB}$  approaches  $90^\circ$ , the slab contribution is nearly zero, and the measured turbulence energy is equivalent with the 2D turbulence. Andrés et al. (2022) also referred the cascade rate for the perpendicular and parallel geometries as the 2D and slab cascade rates, respectively, and found that the 2D heating rate dominates. Telloni et al. (2019) and Zhao et al. (2020) identified a Kolmogorov-like spectrum of unidirectionally propagating Alfvén waves at 1 au and near the Sun in solar wind flows highly aligned with the magnetic field. Similarly, Zank et al. (2022) argued that 2D component does not contribute significantly to the observed slab component in the sub- and super-Alfvén region near the Alfvén surface during encounter 8 of the PSP, where the geometry between the background fields is parallel. This description is consistent with the NI MHD theory (Zank et al. 2017; Adhikari et al. 2022) and the slab + 2D model (Matthaeus et al. 1990; Adhikari et al. 2022), according to which Alfvén waves and 2D turbulence are good candidates for the slab and 2D components.

We used the NI MHD turbulence transport theory (Zank et al. 2017) to calculate the theoretical turbulence cascade rates. In the NI MHD approximation in a low plasma beta regime, the leading order component is 2D MHD fluctuations. The NI MHD turbulence transport model equations have been used successfully to describe the observed features of solar wind turbulence from the inner to the outer heliosphere (Zank et al. 2017, 2018a, 2018b, 2021; Adhikari et al. 2017a, 2020a; Nakanotani et al. 2020; Telloni et al. 2022). We found that PSP measured the slab rather than the 2D turbulence cascade near perihelion on its first orbit. However, SoLO measures both 2D and slab turbulence cascade rates frequently. The general agreement is found between the theoretical and observed 2D and slab turbulence cascade rates as a function of heliocentric distance in the inner heliosphere. We summarize our findings as follows.

1. We found from the PSP measurements at  $\sim 66.3 R_\odot$ , and the SoLO measurements at  $\sim 176.3 R_\odot$  that transverse turbulence cascade rates corresponding to transverse total turbulence energy, transverse Elsässer energies, and transverse fluctuating magnetic energy density and kinetic energy increase as a function of flow-magnetic field obliquity from about  $\theta_{UB} = 10^\circ$  to  $\theta_{UB} = 100^\circ$ . This indicates that the 2D heating rate is larger than the slab heating rate in the inner heliosphere, consistent with what Andrés et al. (2022) found (see also Oughton & Matthaeus 2005; MacBride et al. 2008; Adhikari et al. 2020a).
2. We found theoretically and observationally as a function of heliocentric distance that the 2D turbulent heating rate

is the primary heating rate in the solar wind and the slab heating rate is secondary.

3. The theoretical 2D, slab, and 2D+slab turbulent cascade rates of total turbulence energy, Elsässer energies, fluctuating magnetic energy density, and fluctuating kinetic energy, and the corresponding observed 2D, slab, and total transverse cascade rates are large near perihelion and decrease with increasing distance.
4. The theoretical and observed results show that the ratio of 2D and 2D+slab turbulence cascade rates of the total turbulence energy, the outward and inward Elsässer energy, the fluctuating kinetic and magnetic energy is more than 60% over the distance  $\sim 36.6\text{--}176.3 R_\odot$ . In contrast, the corresponding ratios of the slab and 2D +slab turbulence cascade rate are less than 40%. This is a further indication that heating by 2D fluctuations is the primary mechanism for heating the solar wind in the inner heliosphere.

The theoretical and observed results show that the 2D heating rate is larger than the slab heating rate in the inner heliosphere consistent with the results of Andrés et al. (2022). The simplest explanation for this is that 2D fluctuations form the largest component of the transverse turbulent fluctuations in the solar wind (Zank & Matthaeus 1992, 1993; Zank et al. 2017, 2020; Adhikari et al. 2022). The observational results presented here, and this consistency with theoretical turbulence transport models suggest strongly that 2D turbulence plays a major role in heating the solar wind (Adhikari et al. 2017a, 2020b, 2021b; Zank et al. 2018b; Nakanotani et al. 2020) and corona (Zank et al. 2018a, 2021; Adhikari et al. 2020a; Telloni et al. 2022). We used the turbulence cascade rate expressions from Adhikari et al. (2021a) to calculate various transverse turbulence heating rates, which is different from the third-order law (Politano & Pouquet 1998a, 1998b). Zhao et al. (2021) also used the expression from Adhikari et al. (2021a) to calculate the turbulent cascade rate from PSP measurements at 0.17 au, and found that the turbulent cascade rate is close to that found by Bandyopadhyay et al. (2020), who used the third-order law and turbulence transport theory. MacBride et al. (2008) developed a perpendicular and parallel turbulent heating rate model using the exact laws. It would be interesting to compare these results with the MacBride et al. (2008) approach and include the BepiColombo measurements.

We acknowledge the partial support of a Parker Solar Probe contract SV4-84017, an NSF EPSCoR RII-Track-1 cooperative agreement OIA-1655280, and NASA awards 80NSSC20K1783 and 80NSSC21K1319. The SWEAP Investigation and this study are supported by the PSP mission under NASA contract NNN06AA01C.

## Appendix Solar Wind + NI MHD Turbulence Transport Model Equations

In this Appendix, we present the solar wind (SW) + NI MHD turbulence transport model equations, which are discussed in detail in Adhikari et al. (2022). The 1D steady-state continuity, momentum, and proton and electron pressure equations are given by,

$$\frac{d}{dr}(r^2\rho U) = 0; \quad (\text{A1})$$

$$\rho U \frac{dU}{dr} = -\frac{dP_p}{dr} - \frac{dP_e}{dr}; \quad (\text{A2})$$

$$U \frac{dP_p}{dr} + \gamma P_p \frac{dU}{dr} + 2\gamma \frac{U}{r} P_p = (\gamma - 1) \times (\nu_{pe}(P_e - P_p) + f_p S_t); \quad (\text{A3})$$

$$U \frac{dP_e}{dr} + \gamma P_e \frac{dU}{dr} + 2\gamma \frac{U}{r} P_e = (\gamma - 1) \times [\nu_{ep}(P_p - P_e) - \nabla \cdot \mathbf{q}_e + (1 - f_p) S_t], \quad (\text{A4})$$

where  $\rho$  is the solar wind mass density,  $U$  the speed,  $P_p$  the thermal proton pressure,  $P_e$  the thermal electron pressure,  $\nu_{pe}$  and  $\nu_{ep}$  the rates of proton–electron Coulomb collisions (Barakat & Schunk 1982; Zank 2014), and  $r$  the heliocentric distance. Equation (9) only includes the thermal proton and electron forces. The parameters  $f_p$  and  $(1 - f_p)$  denote the fraction of turbulence energy that heats the solar wind protons, and electrons, respectively, and  $\gamma (= 5/3)$  is the polytropic index. The electron density  $n_e$  and the proton density  $n_p$  are assumed to be equal. The rate of proton–electron Coulomb collisions is given by Cranmer et al. (2009),

$$\nu_{pe} \approx 8.4 \times 10^{-9} \left( \frac{n_e}{2.5 \text{ cm}^{-3}} \right) \left( \frac{T_e}{10^5 \text{ K}} \right)^{-3/2} \text{ s}^{-1}. \quad (\text{A5})$$

The Coulomb collisional frequencies are assumed to be equal for protons and electrons, i.e.,  $n_e \nu_{ep} \sim n_p \nu_{pe}$ . The electron heat flux  $q_e$  is given by the empirical formula (Cranmer et al. 2009),

$$\ln \left( \frac{q_{||,e}}{q_0} \right) = -0.7037 - 2.115x - 0.2545x^2, \quad (\text{A6})$$

which was obtained by fitting the observed electron heat flux from Helios 2 over the distance 0.3–1 au (Pilipp et al. 1990). Here,  $x \equiv \ln(r/1\text{au})$  and  $q_0 = 0.01 \text{ erg cm}^{-2} \text{ s}^{-1}$ .

The turbulent heating term  $S_t$  can be expressed as,

$$S_t = \alpha m_p n_s \left[ \frac{\langle z^{\infty+2} \rangle \langle z^{\infty-2} \rangle^{1/2}}{\lambda_{\infty}^+} + \frac{\langle z^{\infty-2} \rangle \langle z^{\infty+2} \rangle^{1/2}}{\lambda_{\infty}^+} + \frac{\langle z^{*+2} \rangle \langle z^{\infty-2} \rangle^{1/2}}{\lambda_{\infty}^+} + \frac{\langle z^{*-2} \rangle \langle z^{\infty+2} \rangle^{1/2}}{\lambda_{\infty}^-} \right], \quad (\text{A7})$$

where  $m_p$  is the proton mass,  $n_s$  is the solar wind proton density, and  $\alpha$  is a von Kármán–Taylor constant. The terms inside the squared bracket [...] correspond to the dissipation of 2D turbulence and NI/slab turbulence.

The evolution of 2D turbulence can be described by 1D steady-state equations as (Zank et al. 2017; Adhikari et al. 2022)

$$U \frac{d\langle z^{\infty\pm 2} \rangle}{dr} + \frac{1}{2} (\langle z^{\infty\pm 2} \rangle + E_D^{\infty}) \left( \frac{dU}{dr} + \frac{2U}{r} \right) = -2\alpha \frac{\langle z^{\infty\pm 2} \rangle \langle z^{\infty\mp 2} \rangle^{1/2}}{\lambda_{\infty}^{\pm}} + 2C_{\text{sh}}^{\pm} \frac{r_0 |\Delta U| V_{A0}^2}{r^2}; \quad (\text{A8})$$

$$U \frac{dE_D^{\infty}}{dr} + \frac{1}{2} (E_D^{\infty} + E_T^{\infty}) \left( \frac{dU}{dr} + \frac{2U}{r} \right) = -\alpha E_D^{\infty} \left( \frac{\langle z^{\infty+2} \rangle^{1/2}}{\lambda_{\infty}^-} + \frac{\langle z^{\infty-2} \rangle^{1/2}}{\lambda_{\infty}^+} \right) + 2C_{\text{sh}}^{E_D} \frac{r_0 |\Delta U| V_{A0}^2}{r^2}; \quad (\text{A9})$$

$$U \frac{d\lambda_{\infty}^{\pm}}{dr} + \frac{E_D^{\infty}}{2\langle z^{\infty\pm 2} \rangle} \left( \frac{\lambda_{\infty}^{\pm}}{2} - \lambda_{\infty}^{\pm} \right) \left( \frac{dU}{dr} + \frac{2U}{r} \right) = 2\beta \langle z^{\infty\mp 2} \rangle^{1/2} - 2\beta C_{\text{sh}}^{\pm} \frac{r_0 |\Delta U| V_{A0}^2}{r^2} \frac{\lambda_{\infty}^{\pm}}{\langle z^{\infty\pm 2} \rangle}; \quad (\text{A10})$$

$$U \frac{d\lambda_D^{\infty}}{dr} + \frac{\langle z^{\infty+2} \rangle}{2E_D^{\infty}} \left( \frac{dU}{dr} + \frac{2U}{r} \right) \left( \lambda_{\infty}^+ - \frac{\lambda_D^{\infty}}{2} \right) + \frac{\langle z^{\infty-2} \rangle}{2E_D^{\infty}} \left( \frac{dU}{dr} + \frac{2U}{r} \right) \left( \lambda_{\infty}^- - \frac{\lambda_D^{\infty}}{2} \right) = \beta \lambda_D^{\infty} \left( \frac{\langle z^{\infty+2} \rangle^{1/2}}{\lambda_{\infty}^-} + \frac{\langle z^{\infty-2} \rangle^{1/2}}{\lambda_{\infty}^+} \right) - 2\beta C_{\text{sh}}^{E_D} \frac{r_0 |\Delta U| V_{A0}^2}{r^2} \frac{\lambda_D^{\infty}}{E_D^{\infty}}. \quad (\text{A11})$$

The first term on the right-hand side (rhs) of Equation (A8) is the nonlinear dissipation term for the 2D Elsässer energies. In Equation (A9), the first term on the rhs defines the decay of the 2D residual energy through the inertial range. The second term on the rhs of Equations (A8) and (A9) is the turbulent shear source with strengths  $C_{\text{sh}}^{\pm}$  and  $C_{\text{sh}}^{E_D}$ . The parameter  $|\Delta U|$  denotes the velocity difference between the fast and slow solar wind speed, and  $V_{A0}$  is the Alfvén velocity at a reference point  $r_0$ . The parameters  $\beta (= \alpha/2)$  and  $\alpha$  are the von Kármán–Taylor constants.

The Parker spiral magnetic field is given by Weber & Davis (1967)

$$B = B_a \left( \frac{r_a}{r} \right)^2 \left[ 1 + \left( \frac{\Omega r}{U} \right)^2 \left( 1 - \left( \frac{r_a}{r} \right)^2 \right)^2 \sin^2 \theta \right]^{1/2}, \quad (\text{A12})$$

where the subscript “a” represents the reference point  $r_a (\approx 10 R_{\odot})$ ,  $B_a = 1.08 \times 10^3 \text{ nT}$ , and  $\Omega = 2.7 \times 10^{-6} \text{ rad s}^{-1}$  is the solar rotation frequency. We choose a colatitude  $\theta = 90^\circ$ .

Similarly, the 1D steady-state transport equations for slab turbulence can be written as (Zank et al. 2017; Adhikari et al. 2022)

$$(U \mp V_A) \frac{d\langle z^{*\pm 2} \rangle}{dr} + \frac{1}{2} \left( \frac{dU}{dr} + \frac{2U}{r} \right) (\langle z^{*\pm 2} \rangle - E_D^*) + 4b \frac{U \pm V_A}{r} E_D^* \mp \frac{1}{2} (\langle z^{*\pm 2} \rangle - E_D^*) \frac{V_A}{\rho} \frac{d\rho}{dr} = -2\alpha \frac{\langle z^{*\pm 2} \rangle \langle z^{\infty\mp 2} \rangle^{1/2}}{\lambda_{\infty}^{\pm}} + 2C_{\text{sh}}^{* \pm} \frac{r_0 |\Delta U| V_{A0}^2}{r^2}; \quad (\text{A13})$$

$$\begin{aligned}
& U \frac{dE_D^*}{dr} + \frac{1}{2} \left( \frac{dU}{dr} + \frac{2U}{r} \right) (E_D^* - E_T^*) + 4b \frac{U}{r} E_T^* \\
& - 4b \frac{V_A}{r} E_C^* - \frac{V_A}{2\rho} \frac{d\rho}{dr} E_C^* \\
& = -\alpha E_D^* \left( \frac{\langle z^{\infty-2} \rangle^{1/2}}{\lambda_\infty^+} + \frac{\langle z^{\infty+2} \rangle^{1/2}}{\lambda_\infty^-} \right) + 2C_{sh}^* E_D \frac{r_0 |\Delta U| V_{A0}^2}{r^2}; \tag{A14}
\end{aligned}$$

$$\begin{aligned}
& (U \mp V_A) \frac{d\lambda_\pm^*}{dr} + \frac{E_D^*}{2\langle z^{*\pm 2} \rangle} \left( \lambda_\pm^* - \frac{\lambda_D^*}{2} \right) \left( \frac{dU}{dr} + \frac{2U}{r} \right) \\
& - 4b \frac{U \pm V_A}{r} \frac{E_D^*}{\langle z^{*\pm 2} \rangle} \left( \lambda_\pm^* - \frac{\lambda_D^*}{2} \right) \\
& \mp \frac{V_A}{2\rho} \frac{d\rho}{dr} \frac{E_D^*}{\langle z^{*\pm 2} \rangle} \left( \lambda_\pm^* - \frac{\lambda_D^*}{2} \right) = 2\beta \frac{\lambda_\pm^*}{\lambda_\infty^\pm} \langle z^{\infty \mp 2} \rangle^{1/2} \\
& - 2\beta C_{sh}^* \frac{r_0 |\Delta U| V_{A0}^2}{r^2} \frac{\lambda_\pm^*}{\langle z^{*\pm 2} \rangle}; \tag{A15}
\end{aligned}$$

$$\begin{aligned}
& U \frac{d\lambda_D^*}{dr} + \left[ \frac{\langle z^{*+2} \rangle}{2E_D^*} \left( \frac{\lambda_D^*}{2} - \lambda_+^* \right) + \frac{\langle z^{*-2} \rangle}{2E_D^*} \left( \frac{\lambda_D^*}{2} - \lambda_-^* \right) \right] \\
& \times \left( \frac{dU}{dr} + \frac{2U}{r} \right) - 4b \frac{U}{r} \frac{E_T^*}{E_D^*} \lambda_D^* \\
& + 4b \frac{V_A}{r} \frac{E_C^*}{E_D^*} \lambda_D^* + \frac{V_A}{2\rho} \frac{d\rho}{dr} \frac{E_C^*}{E_D^*} \lambda_D^* \\
& + 4b \frac{U}{r} \frac{\langle z^{*+2} \rangle \lambda_+^* + \langle z^{*-2} \rangle \lambda_-^*}{E_D^*} \\
& - 4b \frac{V_A}{r} \frac{\langle z^{*+2} \rangle \lambda_+^* - \langle z^{*-2} \rangle \lambda_-^*}{E_D^*} \\
& - \frac{V_A}{2\rho} \frac{d\rho}{dr} \frac{\langle z^{*+2} \rangle \lambda_+^* - \langle z^{*-2} \rangle \lambda_-^*}{E_D^*} \\
& = \beta \lambda_D^* \left( \frac{\langle z^{\infty-2} \rangle^{1/2}}{\lambda_\infty^+} + \frac{\langle z^{\infty+2} \rangle^{1/2}}{\lambda_\infty^-} \right) \\
& - 2\beta C_{sh}^* E_D \frac{r_0 |\Delta U| V_{A0}^2}{r^2} \frac{\lambda_D^*}{E_D^*}, \tag{A16}
\end{aligned}$$

where  $V_A$  is the Alfvén velocity. Parameter  $b$  describes the geometry of NI/slab turbulence and is related to the closure assumption for the off-diagonal two-point correlations. In Equation (A13), the first term on the rhs is the nonlinear dissipation term for the slab energy in forward and backward propagating modes. On the rhs of Equation (A14), the first term defines the decay of the slab residual energy. The second term on the rhs of Equations (A13) and (A14) is the shear source of turbulence for the slab energy in forward/backward propagating modes, and the residual energy with strengths  $C_{sh}^{\pm}$  and  $C_{sh}^* E_D$ , respectively.

### ORCID iDs

L. Adhikari <https://orcid.org/0000-0003-1549-5256>  
G. P. Zank <https://orcid.org/0000-0002-4642-6192>  
L.-L. Zhao <https://orcid.org/0000-0002-4299-0490>

D. Telloni <https://orcid.org/0000-0002-6710-8142>

### References

- Adhikari, L., Zank, G. P., Bruno, R., et al. 2015, *ApJ*, **805**, 83  
Adhikari, L., Zank, G. P., Hunana, P., et al. 2017a, *ApJ*, **841**, 85  
Adhikari, L., Zank, G. P., Telloni, D., et al. 2017b, *ApJ*, **851**, 117  
Adhikari, L., Zank, G. P., & Zhao, L. 2021a, *Fluid*, **6**, 368  
Adhikari, L., Zank, G. P., Zhao, L. L., Nakanotani, M., & Tasnim, S. 2021b, *A&A*, **650**, A16  
Adhikari, L., Zank, G. P., & Zhao, L. L. 2020a, *ApJ*, **901**, 102  
Adhikari, L., Zank, G. P., Zhao, L. L., et al. 2020b, *ApJS*, **246**, 38  
Adhikari, L., Zank, G. P., Zhao, L. L., & Telloni, D. 2022, *ApJ*, **933**, 56  
Adhikari, L., Zank, G. P., Zhao, L. L., et al. 2021c, *A&A*, **656**, A6  
Andrés, N., Sahraoui, F., Galtier, S., et al. 2019, *PhRvL*, **123**, 245101  
Andrés, N., Sahraoui, F., Huang, S., Hadid, L. Z., & Galtier, S. 2022, *A&A*, **661**, A116  
Bale, S. D., Goetz, K., Harvey, P. R., et al. 2016, *SSRv*, **204**, 49  
Bandyopadhyay, R., Chasapis, A., Chhiber, R., et al. 2018, *ApJ*, **866**, 81  
Bandyopadhyay, R., Goldstein, M. L., Maruca, B. A., et al. 2020, *ApJS*, **246**, 48  
Bandyopadhyay, R., & McComas, D. J. 2021, *ApJ*, **923**, 193  
Barakat, A. R., & Schunk, R. W. 1982, *PIPh*, **24**, 389  
Batchelor, G. K. 1953, *The Theory of Homogeneous Turbulence* (Cambridge: Cambridge Univ. Press)  
Belcher, J. W., & Davis, L., Jr. 1971, *JGR*, **76**, 3534  
Bieber, J. W., Wanner, W., & Matthaeus, W. H. 1996, *JGR*, **101**, 2511  
Breech, B., Matthaeus, W. H., Minnie, J., et al. 2008, *JGRA*, **113**, 8105  
Coleman, P. J., Jr. 1968, *ApJ*, **153**, 371  
Cramer, S. R., Matthaeus, W. H., Breech, B. A., & Kasper, J. C. 2009, *ApJ*, **702**, 1604  
Dasso, S., Milano, L. J., Matthaeus, W. H., & Smith, C. W. 2005, *ApJL*, **635**, L181  
Forman, M. A., Wicks, R. T., & Horbury, T. S. 2011, *ApJ*, **733**, 76  
Galtier, S., & Banerjee, S. 2011, *PhRvL*, **107**, 134501  
Goldreich, P., & Sridhar, S. 1995, *ApJ*, **438**, 763  
Hellinger, P., Papini, E., Verdini, A., et al. 2021, *ApJ*, **917**, 101  
Horbury, T. S., Forman, M., & Oughton, S. 2008, *PhRvL*, **101**, 175005  
Horbury, T. S., O'Brien, H., Carrasco Blazquez, I., et al. 2020, *A&A*, **642**, A9  
Iroshnikov, P. S. 1964, *SvA*, **7**, 566  
Kasper, J. C., Abiad, R., Austin, G., et al. 2016, *SSRv*, **204**, 131  
MacBride, B. T., Smith, C. W., & Forman, M. A. 2008, *ApJ*, **679**, 1644  
Matthaeus, W. H., Dasso, S., Weygand, J. M., et al. 2005, *PhRvL*, **95**, 231101  
Matthaeus, W. H., Ghosh, S., Oughton, S., & Roberts, D. A. 1996, *JGR*, **101**, 7619  
Matthaeus, W. H., Goldstein, M. L., & Roberts, D. A. 1990, *JGR*, **95**, 20673  
Matthaeus, W. H., Zank, G. P., Smith, C. W., & Oughton, S. 1999, *PhRvL*, **82**, 3444  
Monin, A. S., & Yaglom, A. M. 1971, *Statistical Fluid Mechanics; Mechanics of Turbulence* (Cambridge, MA: MIT Press)  
Montgomery, D. 1982, *PhyS*, **1982**, 83  
Nakanotani, M., Zank, G. P., Adhikari, L., et al. 2020, *ApJL*, **901**, L23  
Ng, C. S., Bhattacharjee, A., Munsri, D., Isenberg, P. A., & Smith, C. W. 2010, *JGRA*, **115**, 2101  
Oughton, S., & Matthaeus, W. H. 2005, *NPGeo*, **12**, 299  
Oughton, S., Matthaeus, W. H., Wan, M., & Osman, K. T. 2015, *Phil. Trans. R. Soc.*, **373**, 24010152  
Owen, C. J., Bruno, R., Livi, S., et al. 2020, *A&A*, **642**, A16  
Pilipp, W. G., Muehlhaeuser, K. H., Miggenrieder, H., Rosenbauer, H., & Schwenn, R. 1990, *JGR*, **95**, 6305  
Pine, Z. B., Smith, C. W., Hollick, S. J., et al. 2020, *ApJ*, **900**, 94  
Podesta, J. J. 2009, *ApJ*, **698**, 986  
Podesta, J. J. 2011, *JGRA*, **116**, A05101  
Politano, H., & Pouquet, A. 1998a, *GeoRL*, **25**, 273  
Politano, H., & Pouquet, A. 1998b, *PhRvE*, **57**, R21  
Saur, J., & Bieber, J. W. 1999, *JGR*, **104**, 9975  
Smith, C. W., Isenberg, P. A., Matthaeus, W. H., & Richardson, J. D. 2006, *ApJ*, **638**, 508  
Smith, C. W., Stawarz, J. E., Vasquez, B. J., Forman, M. A., & MacBride, B. T. 2009, *PhRvL*, **103**, 201101  
Smith, C. W., & Vasquez, B. J. 2021, *FRASS*, **7**, 114  
Telloni, D., Adhikari, L., Zank, G. P., et al. 2022, *ApJ*, **929**, 98  
Telloni, D., Carbone, F., Bruno, R., et al. 2019, *ApJ*, **887**, 160  
Usmanov, A. V., Matthaeus, W. H., Breech, B. A., & Goldstein, M. L. 2011, *ApJ*, **727**, 84

- Vasquez, B. J., Smith, C. W., Hamilton, K., MacBride, B. T., & Leamon, R. J. 2007, *JGRA*, **112**, [A07101](#)
- von Karman, T., & Howarth, L. 1938, *RSPSA*, **164**, 192
- Wang, X., Tu, C., & He, J. 2019, *ApJ*, **871**, 93
- Weber, E. J., & Davis, L., Jr. 1967, *ApJ*, **148**, 217
- Yeung, P. K., & Zhou, Y. 1997, *PhRvE*, **56**, 1746
- Zank, G. P. 2014, in *Lecture Notes in Physics*, Vol. 877, *Transport Processes in Space Physics and Astrophysics*, ed. G. P. Zank (Berlin: Springer)
- Zank, G. P., Adhikari, L., Hunana, P., et al. 2017, *ApJ*, **835**, 147
- Zank, G. P., Adhikari, L., Hunana, P., et al. 2018a, *ApJ*, **854**, 32
- Zank, G. P., Adhikari, L., Zhao, L. L., et al. 2018b, *ApJ*, **869**, 23
- Zank, G. P., Dosch, A., Hunana, P., et al. 2012, *ApJ*, **745**, 35
- Zank, G. P., & Matthaeus, W. H. 1992, *JGR*, **97**, 17189
- Zank, G. P., & Matthaeus, W. H. 1993, *PhFI*, **5**, 257
- Zank, G. P., Matthaeus, W. H., & Smith, C. W. 1996, *JGR*, **101**, 17093
- Zank, G. P., Nakanotani, M., Zhao, L. L., Adhikari, L., & Telloni, D. 2020, *ApJ*, **900**, 115
- Zank, G. P., Zhao, L. L., Adhikari, L., et al. 2021, *PhPI*, **28**, 080501
- Zank, G. P., Zhao, L. L., Adhikari, L., et al. 2022, *ApJL*, **926**, L16
- Zhao, L. L., Zank, G. P., Adhikari, L., & Nakanotani, M. 2022a, *ApJL*, **924**, L5
- Zhao, L. L., Zank, G. P., Telloni, D., et al. 2022b, *ApJL*, **928**, L15
- Zhao, L. L., Zank, G. P., Adhikari, L., et al. 2020, *ApJ*, **898**, 113
- Zhao, L. L., Zank, G. P., He, J. S., et al. 2021, *ApJ*, **922**, 188